FERROELECTRICS

Observation of one-dimensional, charged domain walls in ferroelectric ZrO_2

Hai Zhong[1,2]†, Shiyu Wang[1,3]†, Qinghua Zhang[1,3]*, Zhuohui Liu[1,4], Donggang Xie[1,3], Jiali Lu[1,4], Shifeng Jin[1], Shufang Zhang[2], Er-jia Guo[1,3], Meng He[1], Can Wang[1,3], Lin Gu[5], Guozhen Yang[1], Kui-juan Jin[1,3]*, Chen Ge[1,3]*

Ferroelectric charged domain walls (CDWs) with nanoscale thickness and bound charges are typically viewed as ultrathin, reconfigurable, and highly conductive two-dimensional components for domain wall nanoelectronics. Dimensional confinement of such polar topological structures has the potential to increase device density and unlock novel functionalities. We report 180° head-to-head and tail-to-tail CDWs exhibiting one-dimensional (1D) characteristics. These 1D CDWs are confined within the polar layers of ferroelectric ZrO_2 and have atomic-scale dimensions in both width and thickness. Quantitative analysis unveils a distinct screening mechanism of these walls whereby bound polarization charges are compensated by self-balancing oxygen occupancy. We demonstrate electric field–driven manipulation of these 1D CDWs, revealing the microscopic coupling between polarization switching and oxygen-ion transport.

Topological structures in ferroelectric materials, including vortices, skyrmions, merons, and hopfions have emergent properties distinct from the parent phase, which have potential applications in electronics (*1*–*3*). Among these, domain walls (DWs) constitute two-dimensional (2D) or quasi-2D topological defects that separate domains with divergent polarization orientations and are classified as either neutral or charged based on the presence of bound charges (*2*, *4*, *5*). Unlike heterogeneous interfaces between different materials (such as p-n junctions), ferroelectric DWs are homogeneous interfaces with nanoscale thickness. Ferroelectric dynamics impart spatial mobility DWs that enable real-time control of their position, density, and orientation (*6*). Furthermore, electronic confinement combined with distinct symmetry and chemical environment endows mobile DWs with diverse functional electric and magnetic properties (*7*, *8*). Thus, domain wall nanoelectronics establishes a new paradigm for nonvolatile memory and logic by utilizing DWs (*8*–*17*), rather than domains, as active elements, demonstrating the concept of "the wall is the device" (*9*).

The perception of DWs as necessarily 2D or quasi-2D entities in bulk crystals and thin films appears to result from the 3D nature of conventional ferroelectrics. Confining the DW dimensionality necessitates implementation within dimensionally confined ferroelectric systems (Fig. 1A), and emerging fluorite ferroelectrics demonstrate promise in this context (*18*–*20*). In these materials, polarization originates from the off-center displacements of three-coordinated polar oxygen atoms (O_P) within the $Pca2_1$ orthorhombic phase, whereas four-coordinated nonpolar oxygen atoms form spacer layers, creating an alternating polar/nonpolar subcell architecture (*21*). Phonon band theory further reveals a vanishingly weak interaction between adjacent polar subcells, with nonpolar spacer layers effectively functioning as zero-thickness neutral DWs (*18*). Despite their nominally 3D crystal structures, fluorite ferroelectrics are more accurately described as stacks of weakly interacting 2D polar layers that enable stable and switchable ferroelectric domains at the subcell limit (Fig. 1B). Stabilizing DWs within such 2D polar layers inherently confines them to a 1D geometry (Fig. 1C), which we expected to enable atomic-scale DW sizes and ultrahigh DW density.

We present a detailed investigation of 1D CDWs in ZrO_2, a representative fluorite ferroelectric. Multislice electron ptychography (MEP) with ultrahigh resolution [~28 picometers (pm)], revealed head-to-head (H-H) and tail-to-tail (T-T) CDWs embedded within the polar layers. The dimensions of these CDWs in terms of width and thickness (<2.7 Å) confirmed their 1D nature. Quantitative analysis of oxygen occupancy near CDWs demonstrated their screening mechanisms, and through in situ electric field manipulation with integrated differential phase contrast scanning transmission electron microscopy (iDPC-STEM), we achieved both electric field–driven motion of 1D head-to-head CDWs and direct visualization of this process. Their dynamic behavior within 2D polar layers suggested the coupling between polarization switching and ionic transport.

1D charged domain walls in ZrO_2

We synthesized freestanding 5-nm ZrO_2 thin films using pulsed laser deposition and transferred them onto transmission electron microscopy (TEM) grids for plan-view imaging after selective etching (*22*) (see fig. S1 for the experimental setup). Initially, atomic-scale characterization was performed with MEP, which provided high light-element contrast and a spatial resolution of several tens of picometers (fig. S2). Moreover, the MEP technique enables the quantification of atomic occupancy by leveraging the linear relationship between the integrated phase and the number of atoms, with the final image intensity exhibiting insensitivity to positional disorder along the atomic column (*23*, *24*). This technique provided high-quality imaging of both the Zr and O sublattices in the ZrO_2 films. As shown in Fig. 1B, nonpolar oxygen ions (orange) occupied centrosymmetric positions within the Zr lattices, whereas polar oxygen ions (red) exhibited off-center displacements. Their alternating arrangement formed a 3D crystal composed of 2D polar sheets.

Both uniformly polarized 2D ferroelectric domains and dimensionally confined CDWs were embedded within the polar layers of ZrO_2 nanocrystals. Representative regions containing H-H and T-T CDWs are presented in Fig. 2, A and B, respectively. The magnified view of the H-H CDW in Fig. 2C revealed its spatial confinement within the polar layers, directly contradicting earlier theoretical predictions of its energetic instability (*25*–*27*). Flanking O_P displacements exhibited upward or downward shifts relative to centrosymmetric positions, whereas at the wall core, two O_P groups simultaneously compressed into a single Zr subcell. Quantitative analysis of displacement (Fig. 2D) confirmed that the wall thickness was merely one subcell, matching standard O_P displacements (~0.54 Å) in adjacent subcells. Similarly, the T-T CDW (Fig. 2E) exhibited an inverted O_P displacement symmetry, with the wall core exhibiting oxygen vacancies (V_O). The corresponding quantification (Fig. 2F) also revealed a subcell-scale thickness. Both H-H and T-T CDWs had $t \approx 2.55$ Å and $w \approx 2.7$ Å (one subcell each), and l scaled with the grain size (here, $l = 5$ nm, matching the film thickness), thus representing truly 1D structures.

Such highly confined wall dimensions are expected to require very high screening charge concentrations to prevent polarization destabilization (*4*). Specifically, for these 1D CDWs with local polarization $P_l \approx 100\ \mu C/cm^2$ and $t \approx 2.55$ Å, we estimated the screening charge concentration as $2P_l/et \approx 4.9 \times 10^{22}\ cm^{-3}$, where e is the elementary charge.

[1]Beijing National Laboratory for Condensed Matter Physics, Institute of Physics, Chinese Academy of Sciences, Beijing, China. [2]School of Physics and Optoelectronic Engineering, Ludong University, Yantai, China. [3]School of Physical Sciences, University of Chinese Academy of Sciences, Beijing, China. [4]College of Materials Science and Opto-Electronic Technology, University of Chinese Academy of Sciences, Beijing, China. [5]Beijing National Center for Electron Microscopy and Laboratory of Advanced Materials, Department of Materials Science and Engineering, Tsinghua University, Beijing, China. ***Corresponding author. Email: zqh@iphy.ac.cn (Q.Z.); kjjin@iphy.ac.cn (K.J.); gechen@iphy.ac.cn (C.G.)** †These authors contributed equally to this work.

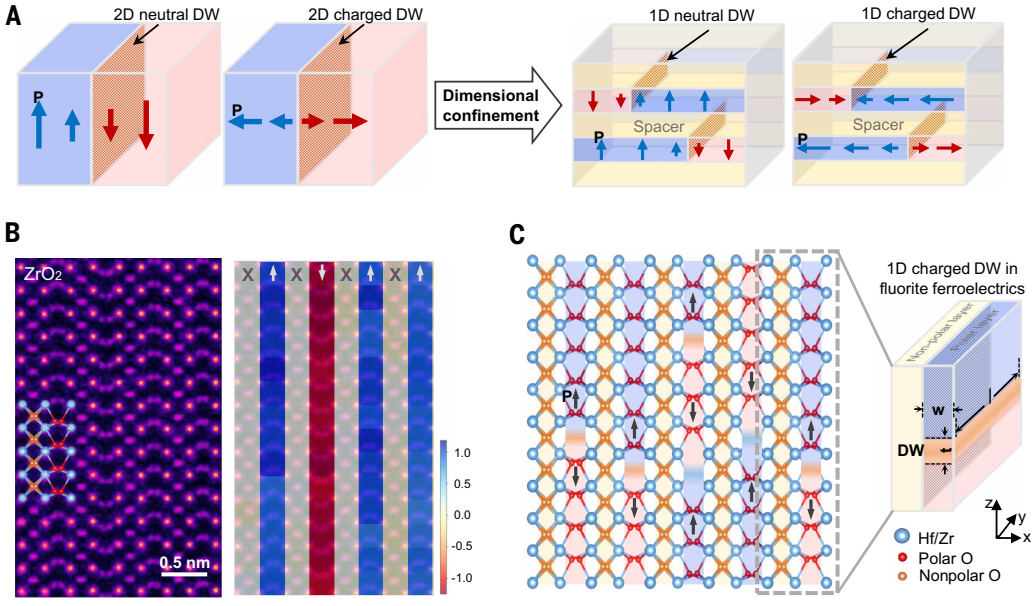

Fig. 1. Concept and realization scheme of 1D domain walls. (**A**) Schematic of dimensional confinement, which reduces the dimensionality of the ferroelectric DWs. (**B**) Projected MEP phase image from ZrO_2 and oxygen displacement mapping. The color scale indicates the normalized displacement relative to the standard $Pca2_1$ structure of ZrO_2. The inset shows the atomic schematic of ferroelectric ZrO_2 along the [010] axis. The arrows denote the polarization directions in the alternating polar/nonpolar subcells, confirming the segmented architecture. (**C**) Atomic schematic of fluorite ferroelectrics (Hf/ZrO_2) with defined 1D CDWs. Geometric parameters of CDWs: thickness (t), width (w), and length (l). 1D character requires $l \gg w \approx t$.

Fig. 2. 1D charged domain walls. Projected MEP phase image containing three H-H CDWs (**A**) and three T-T CDWs (**B**); white boxes indicate the positions of the CDWs. (**C**) Magnified view of DW2 from (A) and the corresponding atomic model. Black arrows denote the displacements of O_P relative to the centrosymmetric positions and gray arrows indicate the local polarization directions. (**D**) Quantitative displacement (D) of O_P in each subcell from (C), demonstrating the H-H wall thickness of one subcell. (**E**) Magnified view of DW1 from (B) and the corresponding atomic model. (**F**) Quantitative displacement of O_P in each subcell from (E), demonstrating the T-T wall thickness of one subcell. Quantitative analysis of oxygen intensities in subcells near the H-H DW2 (**G**) and T-T DW1 (**H**). The total oxygen intensities in the CDW subcell were >1.0 (G) and <1.0 (H), respectively.

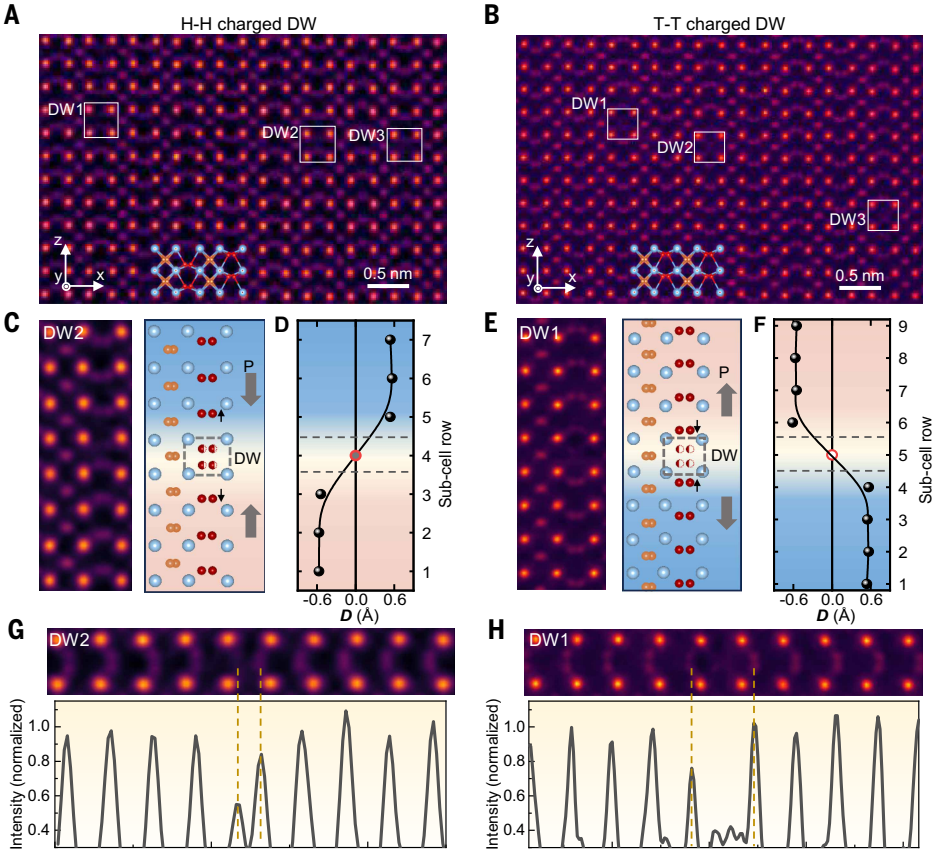

Considering that each oxygen ion or vacancy carries two negative or positive charges and the subcell volume is $V \approx 2.55\ \text{Å} \times 2.71\ \text{Å} \times 5.07\ \text{Å} = 3.50 \times 10^{-23}\ \text{cm}^3$, it can be estimated that complete compensation of these CDWs would require approximately 0.86 oxygen ions or vacancies per subcell. The value of charge concentration approached the metallic free electron densities, indicating that these 1D CDWs may function with excellent conductivity. Characterizing the electrical conductivity of these channels will likely be challenging because of their extremely small size. However, the ultimate size of CDWs demonstrated here will substantially enhance the theoretical density limit of DW-based nonvolatile ferroelectric memories.

To elucidate the charge screening mechanisms of these CDWs, a quantitative analysis of oxygen occupancy was conducted. We first performed quantitative simulations of the projected oxygen atoms along single columns to establish the relation between oxygen occupancy and the MEP phase (fig. S3), thereby determining the occupancy at individual polar oxygen sites near the CDWs. The results indicated that the combined occupancy of the oxygen within the same subcell exceeds 1.0 (Fig. 2G and table S1), demonstrating oxygen over stoichiometry at the domain walls. Furthermore, the depth-resolved analysis (fig. S4) demonstrated that all slices exhibit similar oxygen locations at the domain walls. This wall configuration resembled a theoretically predicted Pbcm structure (*28*), in which excess oxygen occupied sites with half occupancy. Nevertheless, we cannot exclude the possibility of an alternative scenario of periodically overlapping polar structures with excess oxygen, given the limitation in depth resolution of MEP. These excess oxygen ions, carrying negative charges, effectively screened the high density of positive bound polarization charges within the walls, thereby stabilizing these energetically unfavorable, strongly CDWs. Conversely, the polarization discontinuity at these 1D CDWs helped maintain a high density of charged nonstoichiometric oxygen occupancy. Correspondingly, the high density of negatively bound polarization charges at the T-T CDWs was screened by positively charged V_O (Fig. 2H and table S2), analogous to the compensation mechanism observed at the T-T CDWs in $BaTiO_3$ (*29*). Quantitative analysis of oxygen occupancy revealed that both the experimentally measured excess oxygen and V_O concentration at the domain walls matched the predicted value. Statistical analysis of the vacancy-free oxygen columns (fig. S5) indicated that the analysis of oxygen excess or deficiency at the CDWs are reliable.

The mutual relations between nonstoichiometric oxygen occupancy and bound polarization charges revealed a robust mechanism that promoted the stability of these energetically unfavorable CDWs in fluorite ferroelectrics. Furthermore, the widespread presence of these nonstoichiometric oxygen occupancies indicated high mobility of oxygen ions in fluorite ferroelectrics. Their migration led to a local oxygen imbalance (either excess or deficiency), and it was precisely the electrical environment created by these local imbalances that stabilized energetically unfavorable, strongly charged DWs. Such local oxygen imbalance was not restricted to existing solely within distinct 2D polar lamellae. Multiple CDWs could coexist within the same polar layer (fig. S6) and further increased the density of the 1D CDWs within the films.

Motion of 1D charged domain walls

During STEM imaging, electron beam irradiation induced net positive charge accumulation in the dielectric layers through beam-solid interactions, which generated a localized electric field sufficient to drive CDWs motion and polarization switching (*30*). As shown in fig. S7, this induced field produced two distinct polarization states in the same nanocrystal. To fully exploit the intrinsic functional properties of these 1D CDWs, the controlled creation, motion, and erasure of these walls are essential. We used electron beam–induced fields to directly manipulate and observe 1D head-to-head CDWs. Fig. 3, A to C, presents iDPC-STEM images of the same region at three time points (with the full sequences in movie S1 and fig. S8). We observed 1D "head-to-head" CDWs emerging in both regions I and II and found that they moved independently, which was a direct consequence of the negligible interlayer coupling mediated by the intervening nonpolar spacer layers (*18*). The CDWs motion involved the predominant atomic displacement of O_p, with the Zr lattices remaining stationary and no appreciable lattice distortion induced despite oxygen overaccumulation at the DWs

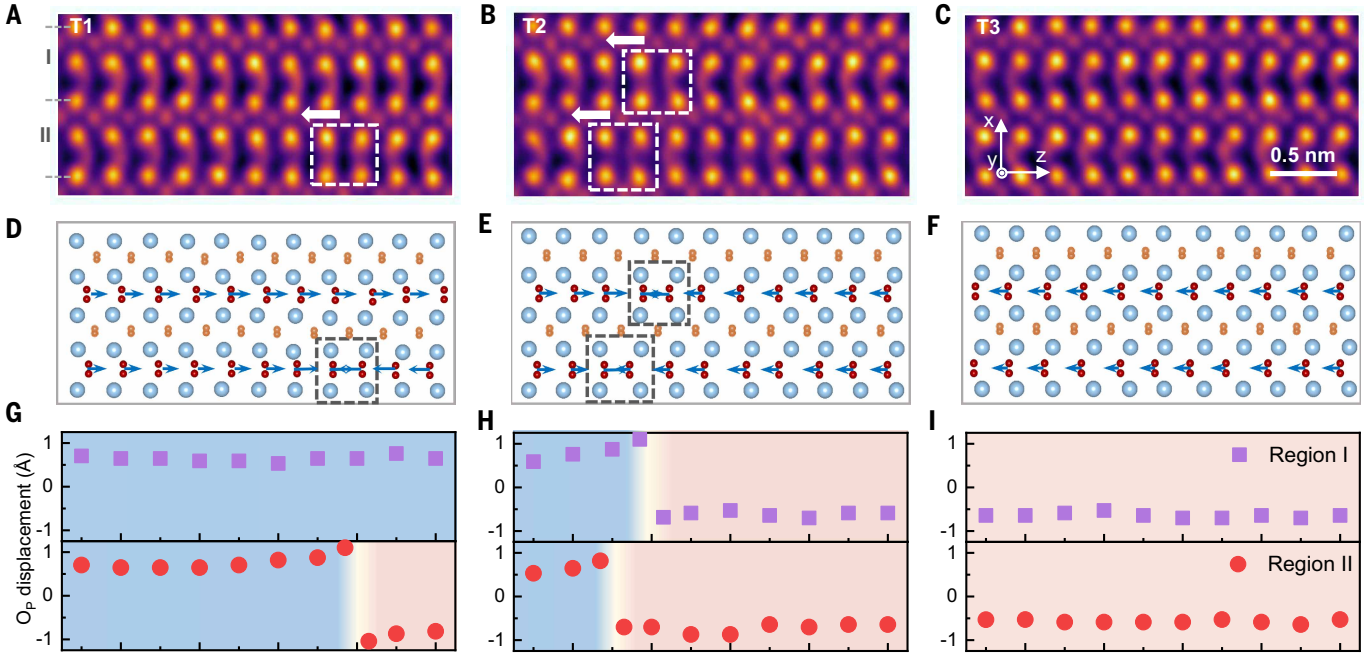

Fig. 3. Motion of 1D H-H CDWs in ZrO_2. (**A** to **C**) Atomic iDPC-STEM frames at three states during CDWs motion. The white dashed boxes mark the CDW positions and the arrows indicate the directions of the CDW motion. (**D** to **F**) Atomic models and polarization mappings corresponding to (A) to (C). The blue arrows denote the local polarization direction (orientation) and magnitude (length). (**G** to **I**) The O_p displacement of each subcell corresponding to (A) to (C).

(fig. S9). The control of 1D CDWs in each polar layer will enable both specific patterns in unit cell–scale and multilevel memory with ultrahigh density. Such multilevel devices are desirable for improving energy efficiency in artificial intelligence and machine learning (*31*).

The exceptional imaging quality enabled the precise atomic localization of both the Zr and O columns, allowing us to quantitatively determine the ionic displacement. Figure 3, D to F, presents the corresponding atomic and polarization mappings at the three time points, with the O_P displacement values of the individual subcells displayed in Fig. 3, G to I. During dynamic motion, we observed that O_P displacements in subcells adjacent to the CDWs exceeded those in remote subcells by up to ~56 pm. This apparent broadening of the H-H CDWs, compared with the single subcell thickness observed in Fig. 2C, likely originated from delayed charge compensation during electric-field–driven wall propagation (*4*). By contrast, the quasistatic CDWs in Fig. 2 maintained a minimal thickness by balancing the oxygen occupancy, which provided sufficient charge compensation.

Coupling between polarization switching and oxygen-ion transport

Given that these 1D H-H CDWs accommodate excess oxygen ions, their propagation simultaneously facilitates oxygen-ion migration. The motion of H-H CDWs mediated both polarization switching and long-range oxygen-ion transport across domains. Indeed, substantial experimental evidence has indicated a strong correlation between polarization and oxygen-ion migration in fluorite ferroelectrics (*32*–*34*), but the atomic-scale dynamics remain elusive. We propose the following microscopic coupling mechanism in which electric field–driven injection of interstitial oxygen ions from grain boundaries and interfaces into polar layers triggers polarization reversal at domain edges, forming H-H CDWs, and subsequent field-driven CDWs motion to the opposite domain boundary effects oxygen expulsion, completing both the polarization switching and oxygen transport cycle (Fig. 4, A to D, and movie S2). Thus, the 2D polar layers in fluorite ferroelectrics function as oxygen-ion conductors, a functionality that is critically dependent on the content of the ferroelectric orthorhombic $Pca2_1$ phase.

To verify this mechanism, we fabricated three sets of samples: (a) $Hf_{0.5}Zr_{0.5}O_2/La_{0.8}Sr_{0.2}MnO_3/SrTiO_3$ (HZO/LSMO/STO), (b) ZrO_2/LSMO/STO, and (c) HZO/indium-tin-oxide (ITO)/yttria-stabilized-zirconia (YSZ), and we systematically characterized their ferroelectric polarization and oxygen-ion conductivity at room temperature. These samples exhibited varying polarization strengths because of their distinct ferroelectric phase content, which was confirmed by positive-up–negative-down measurements (fig. S10). The oxygen-ion conductivity was extracted from the AC impedance spectra under different bias voltages, with careful consideration of electronic conduction (Fig. 4E and fig. S11). The Nyquist plots of all samples exhibited multiple characteristic semicircles attributable to oxygen-ion conduction, demonstrating a strong bias-voltage dependence. The observed dependence of ionic conductivity on electric field can be well-explained by Merz's law (*35*, *36*), which characterizes the velocity of the ferroelectric DW motion (Fig. 4F).

Samples a and b exhibited the activation of both oxygen-ion conduction and macroscopic polarization at 3 to 4 V and showed a positive correlation between the polarization strength and ionic conductivity. Although nonferroelectric sample c showed no polarization, measurable conductivity was observed at high biases, likely caused by field-driven V_O migration (*37*). Notably, the room-temperature oxygen-ion conductivity exceeding 10^{-6} S/cm in sample a surpassed that of most conventional solid oxide electrolytes, including YSZ and CeO_2 (*38*, *39*). This observation agreed with previous reports showing similar impedance behavior in monoclinic HZO and YSZ, whereas orthorhombic HZO exhibits lower impedance modulus (*40*).

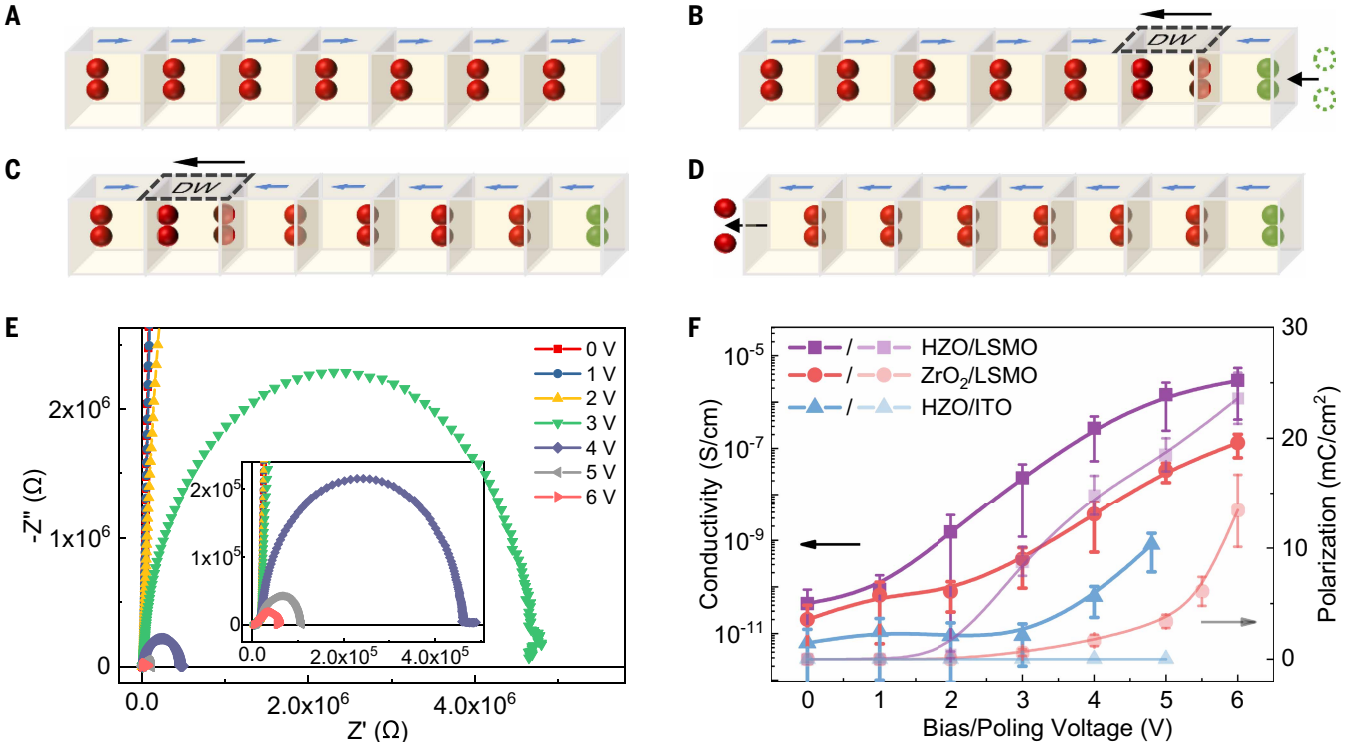

Fig. 4. Coupled CDW motion and oxygen transport in fluorite ferroelectrics. (**A** to **D**) Schematic illustrations of H-H CDW creation (B), motion (C), and erasure (D), demonstrating concurrent polarization switching and cross-domain oxygen transport. Blue arrows denote the local polarization direction of each subcell and black arrows indicate the DW motion direction. (**E**) Nyquist plots of the Pt/HZO/LSMO/STO heterostructure under varying bias voltages at room temperature. (**F**) Bias/poling voltage dependence of oxygen-ion conductivity (left axis) and polarization (right axis).

Discussion

We showed that in fluorite ferroelectrics, not only do 2D 180° neutral DWs nonpolar spacer layers exhibit a thickness of one subcell, often termed "zero-thickness walls" (*18*), but 1D 180° CDWs also attained the ultimate thickness limit of a single subcell. This extreme confinement likely originated from their distinctive screening mechanism. Specifically, in conventional perovskite ferroelectrics, the bound polarization charges at CDWs are primarily compensated by free electrons (or holes), in which the gradient energy in Landau theory and the large effective correlation energy arising from the kinetic energy of the gas of screening electrons collectively govern the 180°CDWs to be typically one order of magnitude thicker than their neutral DWs (*4*, *5*). This theoretical prediction was experimentally confirmed by TEM imaging of 180° CDWs in $Pb(Zr,Ti)O_3$, revealing a thickness of ~7 nm (*41*).

By contrast, fluorite ferroelectrics host oxygen ions and vacancies with substantial mobility within a robust cation framework. These species, which could be negatively or positively charged, efficiently compensated for bound polarization charges at CDWs, which enabled DW stabilization at atomic-scale thickness. Crucially, the off-center displacements of these mobile oxygen ions underlie the polarity of fluorite ferroelectrics, thereby enabling the field-driven motion of 1D CDWs to mediate polarization switching while simultaneously accomplishing cross-domain oxygen-ion transport.

The atomic-scale size and facile electric-field tunability of 1D CDWs in fluorite ferroelectrics offer potential for next-generation nanoelectronic device designs. Similar 1D CDW configurations may extend beyond fluorite ferroelectrics and emerge in other materials with subunit cell–segmented ferroelectricity (e.g., $SrFeO_{2.5}$) (*42*), potentially advancing domain wall nanoelectronics based on dimensionally confined CDWs. Furthermore, the motion of these 1D CDWs carrying oxygen ions or vacancies reveals the intrinsic coupling between oxygen-ion transport and polarization switching. These insights, alongside related findings such as the atomic-scale confinement of CDW pairs by Afroze *et al*. (*43*), highlight the growing potential of dimensionally confined charge orders in ferroelectrics.

REFERENCES AND NOTES

1. J. Junquera *et al.*, *Rev. Mod. Phys.* **95**, 025001 (2023).
2. G. F. Nataf *et al.*, *Nat. Rev. Phys.* **2**, 634–648 (2020).
3. J. Seidel, *Nat. Mater.* **18**, 188–190 (2019).
4. P. S. Bednyakov, B. I. Sturman, T. Sluka, A. K. Tagantsev, P. V. Yudin, *NPJ Comput. Mater.* **4**, 65 (2018).
5. T. Sluka, P. Bednyakov, P. Yudin, A. Crassous, A. Tagantsev, in *Topological Structures in Ferroic Materials: Domain Walls, Vortices and Skyrmions*, J. Seidel, Ed. (Springer, 2016), pp. 103–138.
6. D. Wang *et al.*, *Nature* **641**, 76–82 (2025).
7. T. Rojac *et al.*, *Nat. Mater.* **16**, 322–327 (2017).
8. D. Meier, S. M. Selbach, *Nat. Rev. Mater.* **7**, 157–173 (2022).
9. G. Catalan, J. Seidel, R. Ramesh, J. F. Scott, *Rev. Mod. Phys.* **84**, 119–156 (2012).
10. P. Sharma, T. S. Moise, L. Colombo, J. Seidel, *Adv. Funct. Mater.* **32**, 2110263 (2022).
11. Z. Liu *et al.*, *Nature* **613**, 656–661 (2023).
12. A. Q. Jiang *et al.*, *Nat. Mater.* **19**, 1188–1194 (2020).
13. X. Chai *et al.*, *Nat. Commun.* **11**, 2811 (2020).
14. P. Sharma *et al.*, *Sci. Adv.* **3**, e1700512 (2017).
15. J. Jiang *et al.*, *Nat. Mater.* **17**, 49–56 (2018).
16. P. Sharma *et al.*, *ACS Appl. Mater. Interfaces* **17**, 2491–2497 (2025).
17. P. Sharma, P. Schoenherr, J. Seidel, *Materials* **12**, 2927 (2019).
18. H.-J. Lee *et al.*, *Science* **369**, 1343–1347 (2020).
19. B. Noheda, P. Nukala, M. Acuautla, *Nat. Mater.* **22**, 562–569 (2023).
20. S. S. Cheema *et al.*, *Nature* **604**, 65–71 (2022).
21. T. S. Böscke, J. Müller, D. Bräuhaus, U. Schröder, U. Böttger, *Appl. Phys. Lett.* **99**, 102903 (2011).
22. H. Zhong *et al.*, *Adv. Mater.* **34**, 2109889 (2022).
23. Z. Dong *et al.*, *Nature* **630**, 847–852 (2024).
24. Z. Chen *et al.*, *Science* **372**, 826–831 (2021).
25. E. D. Grimley, T. Schenk, T. Mikolajick, U. Schroeder, J. M. LeBeau, *Adv. Mater. Interfaces* **5**, 1701258 (2018).
26. Z. Xu, X. Zhu, G.-D. Zhao, D. W. Zhang, S. Yu, *Appl. Phys. Lett.* **124**, 012902 (2024).
27. T. K. Paul, A. K. Saha, S. K. Gupta, *Sci. Rep.* **14**, 9861 (2024).
28. X. Sang, E. D. Grimley, T. Schenk, U. Schroeder, J. M. LeBeau, *Appl. Phys. Lett.* **106**, 162905 (2015).
29. U. Petralanda, M. Kruse, H. Simons, T. Olsen, *Phys. Rev. Lett.* **127**, 117601 (2021).
30. S. Calderon V *et al.*, *Science* **380**, 1034–1038 (2023).
31. M. Rao *et al.*, *Nature* **615**, 823–829 (2023).
32. M. O. Hill *et al.*, *Adv. Mater.* **36**, e2408572 (2024).
33. P. Nukala *et al.*, *Science* **372**, 630–635 (2021).
34. M. Shao *et al.*, *Nano Lett.* **24**, 1231–1237 (2024).
35. S. Liu, I. Grinberg, A. M. Rappe, *Nature* **534**, 360–363 (2016).
36. G.-D. Zhao *et al.*, arXiv:2302.02874 [cond-mat.mtrl-sci] (2023).
37. P. Gao *et al.*, *J. Am. Chem. Soc.* **132**, 4197–4201 (2010).
38. H. R. Khakhal *et al.*, *Mater. Sci. Eng. B* **297**, 116675 (2023).
39. I. Garbayo *et al.*, *J. Mater. Chem. A Mater. Energy Sustain.* **7**, 25772–25778 (2019).
40. E. Barriuso *et al.*, *Adv. Electron. Mater.* **10**, 2300522 (2024).
41. C.-L. Jia *et al.*, *Nat. Mater.* **7**, 57–61 (2008).
42. J. Jang *et al.*, *Nat. Mater.* **24**, 1228–1235 (2025).
43. N. Afroze *et al.*, arXiv:2507.18920 [cond-mat.mtrl-sci] (2025).

ACKNOWLEDGMENTS

Funding: This work was supported by the National Key R&D Program of China (2024YFA1409500); the National Natural Science Foundation of China (grants 12222414, 52322212, 12174437, 52025025, 52421001, 52250402, and 12304123); the Youth Innovation Promotion Association of CAS (Y2022003); the Youth Innovation Technology Project of Higher School in Shandong Province (2023KJ211); and project ZR2023QA085 supported by Shandong Provincial Natural Science Foundation. **Author contributions:** C.G. and Q.Z. conceived the idea of the work. H.Z. and Z.L. fabricated thin films. S.W. and Q.Z. performed and analyzed the STEM experiments. The device fabrication and measurements were done by H.Z. with support from D.X., J.L., S.J., and S.Z. H.Z., S.W., Q.Z., and C.G. prepared the manuscript. E.G., M.H., C.W., K.J., and G.Y. participated in the discussion of manuscript. C.G., Q.Z., K.J., and L.G. supervised the project. **Competing interests:** Authors declare that they have no competing interests. **Data, code, and and materials availability:** All data and details of materials synthesis are available in the main text or the supplementary materials.

SUPPLEMENTARY MATERIALS

science.org/doi/10.1126/science.aeb7280
Materials and Methods; Figs. S1 to S11; Tables S1 and S2; References (*44*–*51*); Movies S1 and S2
Submitted 24 August 2025; accepted 3 December 2025
10.1126/science.aeb7280